

Static Aeroelastic Model Validation of Membrane Micro Air Vehicle Wings

Bret Stanford* and Michael Sytsma†

University of Florida, Gainesville, Florida 32611-6250

Roberto Albertani‡

University of Florida, Shalimar, Florida 32579-6250

Dragos Viieru§ and Wei Shyy¶

University of Michigan, Ann Arbor, Michigan, 48109-2140

and

Peter Ifju**

University of Florida, Gainesville, Florida 32611-6250

DOI: 10.2514/1.30003

A low-aspect-ratio, low-Reynolds-number membrane wing has been identified as a viable platform for micro air vehicle applications. Desirable flying qualities include high lift and larger stability margins. Several challenges are associated with the numerical modeling of such a wing, including highly three-dimensional flows, separation bubbles, and nonlinear membrane behavior. A thorough model validation and system identification effort is therefore required. A novel experimental setup integrates a wind tunnel with a visual image correlation system for simultaneous measurement of wing displacements, strains, and aerodynamic loads. These three metrics are used for a direct comparison of numerical and experimental data for both pre- and poststall angles of attack. Suitable correspondence is demonstrated for moderate angles of attack; methods for increasing the model fidelity can be made for angles with poor predictive capability. Computed flow structures reveal further information concerning the aeroelastic behavior of membrane wings.

Nomenclature

α	=	angle of attack
b	=	span
C_D	=	coefficient of drag
C_L	=	coefficient of lift
C_m	=	coefficient of pitching moment
C_p	=	coefficient of pressure
c	=	chord
$\varepsilon_{xx}, \varepsilon_{yy}, \varepsilon_{xy}$	=	plane strains
Re	=	Reynolds number
U_∞	=	freestream velocity
u, v, w	=	Cartesian displacements
x, y, z	=	Cartesian coordinates

I. Introduction

A HALLMARK of many practical micro air vehicle (MAV) designs is a thin, cambered, low-aspect-ratio wing (typically on the order of 1). This approach maximizes the wing area for a given size constraint (150 mm, by definition), thus improving the flight

duration for a given payload (which will include motors, actuation servos, and receivers and which may include video cameras or autopilot systems). Further desire to minimize the size of a MAV has led to the elimination of horizontal stabilizers, providing a “flying wing.” Such a wing requires a reflex airfoil for stability, wherein the recurve present toward the trailing edge (negatively cambered) can help offset the longitudinal pitching moment of the remainder of the wing. High-velocity electric motors power small propellers (in either a puller or a tractor configuration) for vehicle propulsion. A successfully designed, fabricated, and flight-tested micro air vehicle can be seen in Fig. 1.

A series of thin, flexible, lightweight materials have been identified as being well suited to the fabrication of micro air vehicles [1]: composite laminates and thin, extensible, latex rubber membranes. The leading edge of the wing seen in Fig. 1 is constructed from a bidirectional plain-weave carbon-fiber laminate, as is the thin curved strip (perimeter) that outlines the planform. The remainder of the wing (outside of the windowed hatch at the root, for access to the payload) is composed of the rubber membrane skin, which is sealed to the carbon fiber with spray adhesive. This combination of carbon-fiber skeleton and membrane skin affords a wing that is lightweight enough to fly in the appropriate flight regime (MAV speeds may reach 13 m/s, which equates to a relatively low Reynolds number of 10^5), but strong enough to sustain the resulting lift forces. Further benefits include durability, ease of fabrication, and, most important, passive shape adaptation.

The MAV wing’s aerodynamic performance is significantly affected by the adaptive inflation (aerodynamic twist) of the latex membrane skin. Desirable aeroelastic effects include higher lift (due to the adaptive camber) and improved longitudinal static stability (as the maximum camber shifts toward the trailing edge). The resulting nonoptimal aerodynamic wing shape (compared with a streamlined rigid wing) will incur a drag penalty, however. This work details the development of a static aeroelastic model of the adaptively inflating membrane MAV wing. Several challenges are associated with such a modeling effort: the low-aspect-ratio wing forces a highly three-dimensional flow, the low Reynolds number implies strong viscous effects such as flow separation/reattachment, and the mechanics of

Presented as Paper 1067 at the 45th AIAA Aerospace Sciences Meeting and Exhibit, Reno, NV, 8–11 January 2007; received 24 January 2007; revision received 26 July 2007; accepted for publication 26 July 2007. Copyright © 2007 by Bret Kennedy Stanford. Published by the American Institute of Aeronautics and Astronautics, Inc., with permission. Copies of this paper may be made for personal or internal use, on condition that the copier pay the \$10.00 per-copy fee to the Copyright Clearance Center, Inc., 222 Rosewood Drive, Danvers, MA 01923; include the code 0001-1452/07 \$10.00 in correspondence with the CCC.

*Research Assistant, Department of Mechanical and Aerospace Engineering.

†Research Assistant, Department of Mechanical and Aerospace Engineering.

‡Visiting Professor, Research and Education Engineering Facility.

§Postdoctoral Research Fellow, Department of Aerospace Engineering.

¶Clarence L. “Kelly” Johnson Collegiate Professor and Chair, Department of Aerospace Engineering.

**Professor, Department of Mechanical and Aerospace Engineering.



Fig. 1 Micro air vehicle using a low-aspect-ratio membrane wing.

the membrane inflation are inherently nonlinear, etc. As such, a series of experimental techniques are used for model validation and system-identification purposes. Finally, both numerical and experimental data (in terms of wing displacements, strain, pressure fields, longitudinal aerodynamic coefficients, and flow structures) will be used to facilitate a greater understanding of the fluid–structure interaction of a membrane micro air vehicle wing.

Numerical modeling of membrane wings is well-represented in the literature. Jackson [2] derived and solved an equation for an extensible two-dimensional sail wing (fixed at the leading and trailing edges) in inviscid flow at an arbitrary angle of attack. Later work by Smith and Shyy [3] studied the same problem with a Reynolds-averaged Navier–Stokes solver. The data indicated that potential flow solvers can provide meaningful insight into the physics of the problem only for small angles of attack and for small membrane excess ratios; otherwise, viscous effects within the surrounding flow dominate. Early work on the aeroelasticity of a three-dimensional membrane wing was conducted by Boudreaux [4]. The author used an inviscid vortex lattice method, and described the wing section shapes as cubic polynomials; the aeroelastic solution was given in terms of the excess length within the fabric. Jackson and Christie [5] used a nonlinear membrane finite element coupled to a vortex lattice method to study a thin triangular sail. They found that fixing the trailing edge for adaptive camber provided the highest lift. Sugimoto [6] found solutions to the static aeroelasticity of a fully restrained (about the leading edge, trailing edge, and wingtips) elastic circular wing and was able to obtain good correlation to experimental results. Lian et al. [7] computed the aeroelasticity of a membrane MAV with three battens imbedded within each wing. A time-dependent Navier–Stokes flow solver was coupled with a nonlinear hyperelastic membrane model. The data indicated that the membrane wing experiences a self-excited vibration on the order of 100 Hz, with a maximum wing velocity of about 2% of the freestream. Camber, incidence, and wing deformation at various span locations are documented as functions of angle of attack.

Early wind-tunnel work by Fink [8] tested a sail wing with a membrane fabric skin. Before stall, the deformation profile of the wing was fairly smooth, but rippling developed as the wing stalled. At low angles of attack, the lift curve was reported to be unusually steep, due to the adaptive camber. Fink noted that the pretension within the wing has a significant effect upon the aerodynamic characteristics. Greenhalgh and Curtiss [9] conducted similar tests with varying planform shapes: triangular, elliptical, and parabolic. They found that for the range of tested flight conditions, only the parabolic planform shape could support the loading without the aid of a trailing-edge support member and exhibited superior aerodynamic performance. Galvao et al. [10] conducted wind-tunnel testing on a latex membrane sheet stretched between two rigid posts. Photogrammetry was used to measure the membrane displacements. As previously discussed, the steep lift slopes were reported, as well as smoother stall behavior. The latter was due to a decambering of the wing, as the pressure over the upper surface

increased due to imminent flow separation. Fleming et al. [11] discussed the use of projection moiré interferometry for measuring the deformation of a low-aspect-ratio membrane MAV wing in a wind tunnel. DeLuca et al. [12] reported the benevolent stall behavior of flexible MAV wings, citing an aerodynamic efficiency 20 to 30% larger than that measured from a rigid wing. MAVs with membrane wings displayed static stability in all three principal control axes, whereas the vehicle with a rigid wing was not definitely stable in any axis.

The remainder of this work is organized as follows. A complete description of all the mechanisms used to provide information pertaining to membrane wing aeroelasticity [closed-loop wind tunnel, strain-gage sting balance, visual image correlation (VIC), finite element analysis (FEA), computational fluid dynamics (CFD), and aeroelastic coupling] will be given, as well as a discussion of the particular MAV prototype used for testing. System identification for the relevant structural parameters will be described, followed by model validation via wing deformation and longitudinal aerodynamic coefficients. Once a suitable level of confidence in the aeroelastic model is obtained, the computed flow structures are discussed in detail.

II. Experimental Techniques

A. Closed-Loop Wind Tunnel

The test facility used for the entirety of this work is an Engineering Laboratory Design, Inc. (ELD) 407B closed-loop wind tunnel, with the flow loop arranged in a horizontal configuration. The test section has an inner dimension of 0.84 m on each side and is 2.44 m deep. The velocity range is between 2 and 45 m/s, and the maximum Reynolds number is 2.7 million. Centerline turbulence levels were measured on the order of 0.2%. Optical access is available on the sidewalls and the ceiling. A Heise model-PM differential pressure transducer is attached to a pitot-static tube located at the center of the section's entrance; the system is capable of measuring wind speeds up to 45 m/s. A four-wire resistance temperature detector mounted to the wall of the test section measures the airflow temperature.

B. Strain-Gage Sting Balance

An Aerolab 01-15 six-component strain-gage sting balance is used to measure the aerodynamic forces and moments of the wind-tunnel models. Each of the six channels is in a full Wheatstone-bridge configuration, with five channels dedicated to forces and one dedicated to a moment. The forces generated during MAV flight may not be more than a few percent of the maximum measurable load of each channel. Electrical signals are on the order of microvolts, which introduces a challenging data processing and signal-conditioning problem. The balance's drag signal, for example, is calibrated down to 0.01 N, which is about 40% of the minimum theoretical drag expected from a MAV. Data acquisition is done with a NI SCXI 1520 eight-channel programmable strain-gage module with full bridge configuration, 2.5 excitation volts, and a gain of 1000. A NI 6052 DAQ PAD FireWire provides A/D conversion, multiplexing, and the PC connection.

For a given flight condition, the output signals from the six components are sampled at 1000 Hz for 2 s. The average of this data is sent to one module for the calculation of the relevant aerodynamic coefficients (C_L , C_D , C_m , etc.), and the standard deviation of the data is stored for an uncertainty analysis. Corrections are applied to the aerodynamic coefficients to account for blockage (solid, wake, and streamline curvature) and flexibility effects. The latter is chiefly caused by the wind-tunnel model's slightly flexible support (strain-gage sting balance). Wind loads cause the model to pitch up in the wind tunnel. Visual image correlation (described next) is used to measure the small rigid-body movement to correct the angle of attack. The sting balance is mounted to a custom-fabricated aluminum model arm within the section. The arm extends through a hole in the section wall and is then attached to a gearbox and a brushless servomotor system for pitching control (rates on the order of 1 deg/s). Tunnel speed, model inclination, and force/moment

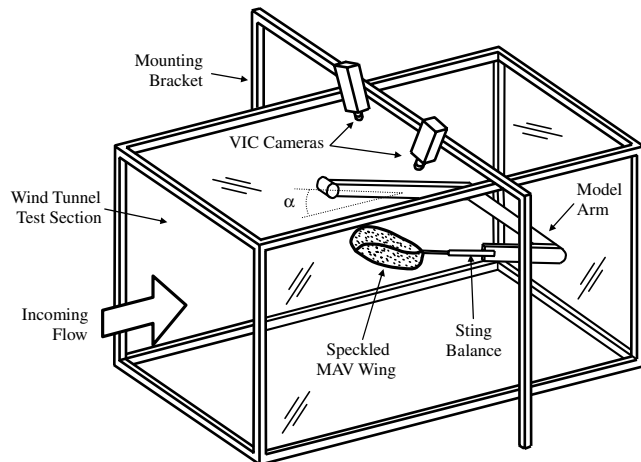


Fig. 2 Schematic of the wind-tunnel setup.

measurements are set/acquired using a dedicated PC and in-house software. A schematic of the wind-tunnel setup can be seen in Fig. 2.

C. Visual Image Correlation

VIC is a noncontacting full-field measurement technique originally developed by researchers at the University of South Carolina [13,14]. The underlying principle is to calculate the displacement field of a test specimen by tracking the deformation of a random speckling pattern applied to the surface. Two precalibrated cameras digitally acquire this pattern before and after loading using stereo-triangulation techniques. The VIC system then tries to find a region (in the image of the deformed specimen) that maximizes a normalized cross-correlation function corresponding to a small subset of the reference image (taken when no load is applied to the structure). The image space is iteratively swept by the parameters of the cross-correlation function to transform the coordinates of the original reference frame to coordinates within the deformed image. Because it is unlikely that the deformed coordinates will directly fall onto the sampling grid of the reference image, accurate gray-value interpolation schemes are implemented to achieve optimal subpixel accuracy without bias.

To capture the three-dimensional features and deformation of a wind-tunnel model, twin synchronized precalibrated cameras, each looking from a different viewing angle, are installed above the wind-tunnel ceiling (seen in Fig. 2). Because the cameras must remain stationary throughout the experiment (to preserve the camera calibration), a mounting bracket straddles the tunnel to prevent the transmission of vibration. Optical access into the test section is through a glass ceiling. Two continuous 250-W lamps illuminate the model, enabling the use of exposure times of 5 to 10 ms. The energy emitted from the lights, a potential hazard for the specimen (particularly, the thin membrane skin, for which the elastic properties are known to degrade in adverse conditions), is not a concern due to the cooling effect of the wind-tunnel flow.

The twin cameras are connected with a PC via an IEEE-1394 FireWire cable, and a specialized unit is used to synchronize the camera triggers for instantaneous shots. A standard acquisition board installed in the computer carries out digitalization of the images, and the image processing is carried out by custom software provided by Correlated Solutions, Inc. Typical data results obtained from the VIC system consist of the geometry of the surface in discrete coordinates x , y , and z and the corresponding displacements u , v , and w . The VIC system places a grid point every N pixels, where N is user-defined. A final postprocessing option involves calculating the in-plane strains ϵ_{xx} , ϵ_{yy} , and ϵ_{xy} . This is done by mapping the displacement field onto an unstructured triangular mesh and conducting the appropriate numerical differentiation (the complete definition of finite strains is used).

The general procedural steps used in this work are as follows:

- 1) Take a picture of the wind-tunnel model at the set angle of attack, with the wind off.
- 2) Start the wind tunnel and wait for stable conditions.
- 3) Take a picture of the deformed wing and record the aerodynamic loads.
- 4) Stop the wind tunnel, move the model to the next angle, and repeat.

Each pair of images is then sent to the VIC system for processing. The acquired displacement field is composed of both the elastic deformation of the wing and the rigid-body motions inherent within the wind-tunnel setup. These motions are thought to primarily originate from the flexibility of the sting balance and must be filtered out. The computed strain field is, theoretically, unaffected by these motions.

D. Specimen Selection and Preparation

Only the wing (125 mm wingspan, 104 mm root chord, and aspect ratio of 1.2) of the MAV seen in Fig. 1 is considered in this work. The camber at the root is 6.8% (at $x/c = 0.22$), the reflex at the root is -1.4% (at $x/c = 0.86$), and 9 deg of positive geometric twist (nose up) is built into the wingtip. The MAV wing has 7 deg of dihedral between $2y/b = 0.4$ and the wingtip. The fuselage, stabilizers, and propeller are omitted from both the computations and experiments. The leading edge, perimeter (curved strip that surrounds the latex membrane wing skin), and inboard portion of the wing are constructed from six layers of plain-weave carbon-fiber plies, each in the ± 45 -deg orientation. Because of weight considerations, this is a thicker laminate than would be implemented for practical MAV design. The excessive stiffness ensures that the majority of strain energy due to aerodynamic loading is within the membrane (rather than bending/twisting of the laminate), thus simplifying the numerical modeling effort. After the curing cycle, the carbon-fiber wing skeleton is painted a light color. A random speckling pattern (black spray paint droplets) is then applied to a sheet of latex rubber. The sheet is stretched about a frame, pinned along the boundary to hold the tension, and then sealed to the laminate skeleton by a spray glue adhesive. After the glue has dried, the excess latex is trimmed away. VIC is used to measure the resulting prestrain in the MAV's membrane wing by taking images of the speckled latex sheet before and after it is adhered to the carbon-fiber wing skeleton.

III. Numerical Techniques

A. Computational Fluid Dynamics

The three-dimensional incompressible Navier–Stokes equations written in curvilinear coordinates are solved for the steady laminar flow over a MAV wing with a span of 125 mm. The fuselage, stabilizers, and propeller are not taken into account. The computational domain can be seen in Fig. 3, with the MAV wing enclosed within. Inlet and outlet boundaries are marked by the flow vectors; velocity is specified at the inlet, and a zero pressure condition is enforced at the outlet. The configuration shown in Fig. 3 is for simulations at a model inclination of 0 deg. For nonzero angles, the lower and upper surfaces will also see a mass flux. The side walls are modeled as slip walls, and thus no boundary layer forms. The MAV wing itself is modeled as a no-slip surface. The dimensions of the computational domain are given in terms of the root chord (104 mm) and are placed far enough away from the MAV surface to not significantly affect the aerodynamics. Because no flow is expected to cross the root chord of the wing (no propeller is modeled), symmetry is exploited by modeling only half of the computational domain (the plane of symmetry is also modeled as a slip wall). A detailed view of the resulting structured mesh (the nodes that lie on the plane of symmetry and the MAV wing) is given in Fig. 3: 210,000 nodes fill half of the computational domain, with 1300 nodes on the wing surface. The Navier–Stokes equations are solved on this mesh using a finite volume formulation. A second-order central-difference operator is used for pressure and diffusive

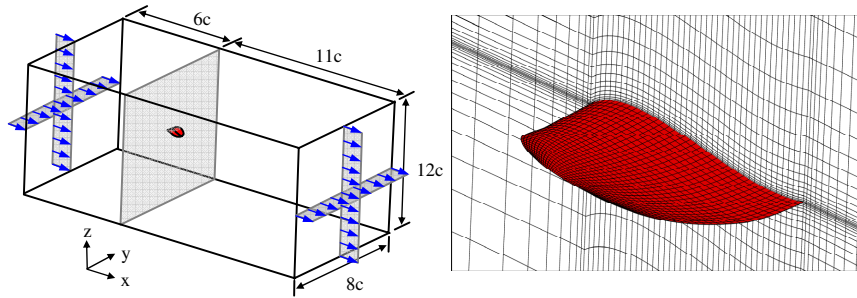


Fig. 3 CFD computational domain (left) and detail of mesh near the wing surface (right).

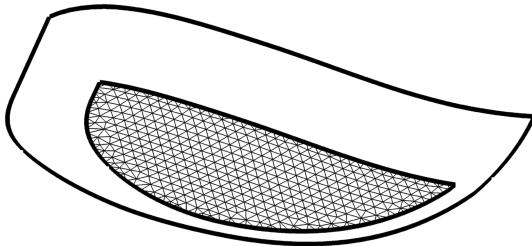


Fig. 4 Finite element mesh of the membrane wing skin.

terms, whereas a second-order upwind scheme handles all convective terms [15].

B. Finite Element Analysis

As discussed previously, the carbon-fiber regions of the MAV wing are built excessively thick out of consideration for modeling simplifications. As such, only the membrane regions of the wing are modeled with the unstructured triangular mesh seen in Fig. 4. The nodes that lie on the perimeter of this mesh are given a zero-displacement boundary condition. Several nonlinearities are included in the finite element formulation: large displacements (both in-plane and out-of-plane motions), finite strains, and redistribution of nonconservative pressure loads due to membrane deformation [16]. Material nonlinearities are ignored for the current work. Although latex rubber is technically a hyperelastic solid (the dependence of the strain energy upon the invariants of the deformation tensor [17] causes a nonlinear stress-strain curve), the strain levels that accumulate are assumed to be small enough (this is validated next) to warrant a linear stress-strain relationship: Hooke's law is used here. Furthermore, the latex rubber is assumed to be isotropic, with equal material properties in all directions.

The effect of the membrane's pretension upon the MAV deformation must also be accounted for in the structural model. A linear stress-stiffening module is used to describe the relationship between the in-plane pretension and the transverse deformation (essentially, Poisson's equation for a pressurized membrane [16]). As discussed previously, VIC is used to measure the prestrain in the membrane. This experimental data field is sent through a moving average smoother and then interpolated onto the triangular mesh of Fig. 4, for use in the structural finite element membrane model. Hooke's law is used to convert these prestrains into prestresses.

C. Aeroelastic Coupling

The steady fluid-structure interaction of the flexible MAV wing is computed in the following manner:

- 1) Solve the 3-D incompressible viscous Navier-Stokes equations for the steady laminar flowfield, using the CFD grid shown in Fig. 3.
- 2) Interpolate the computed wing pressures onto the FEA grid shown in Fig. 4.
- 3) Solve for the resulting wing displacements using the structural membrane model.
- 4) Interpolate the displacement onto the MAV wing of the CFD grid.

- 5) Remesh the CFD grid using a master/slave moving-grid scheme [7].

- 6) Repeat steps 1-5 until convergence is achieved: less than 0.1% change in maximum displacement.

Less than ten iterations are usually adequate for simulations at moderate angles of attack ($3 \text{ deg} < \alpha < 18 \text{ deg}$), though up to 20 may be needed for angles outside of this range. Step 1 requires between 150 and 250 subiterations, whereas step 3 can typically converge within 10 subiterations.

IV. Results and Discussion

A. Membrane Prestrain

The amount of prestrain injected into the membrane skin represents an aeroelastic tailoring problem. If the lift-to-drag ratio is an important design metric, then a taut membrane (with high prestrain) is preferred. This will prevent the drag penalty that ensues with excessive wing deformation. The advantage of a thin membrane wing skin (as opposed to a homogenous carbon-fiber wing) is then only realized from a weight-savings standpoint. If large longitudinal static stability is required, then the membrane should be slack. For the current work, a moderate amount of prestrain is used, by stretching a square of latex rubber (150 mm on each side) biaxially: 4 mm in both the chordwise and the spanwise directions. The taut membrane is then adhered to the wing surface and VIC is used to measure the prestrain fields, shown in Fig. 5. The anisotropy of the tension is clearly evident. A state of isotropic biaxial tension (with no shear) is very difficult to obtain; the size of the taut membrane sheet is not significantly larger than the MAV wing surface, and thus the prestrain is distorted by end effects. Transferring a state of isotropic tension in a flat membrane to a wing surface with camber and dihedral provides further complications. As such, the prestrain fields in the membrane wing are used in a passive sense; the general magnitude of the prestrain can be controlled, but not (with current MAV fabrication methods) the distribution. As described previously, a linear Hooke's law is used to convert these prestrains into prestresses.

B. Structural Model System Identification

Calibration of the structural model is done by applying a known load to the taut membrane MAV skin and tuning the material

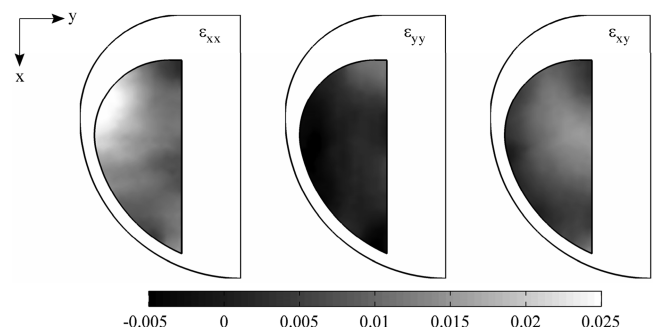


Fig. 5 Chordwise (left), spanwise (center), and shear (right) membrane prestrain fields.

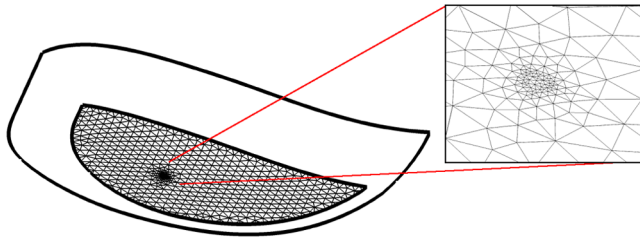


Fig. 6 Refined finite element mesh suitable for a concentrated transverse force.

parameters to achieve suitable correspondence between numerical and experimental deformation fields. Weights are hung from the end of a thin string glued to the center of the membrane skin. Although the experimental setup is trivial, such a concentrated force can create a singularity within the membrane skin; numerical modeling must be conducted with care. A separate set of finite element meshes are built with a large mesh density around the loading region, an example of which can be seen in Fig. 6. The thin string is assumed to act as a distributed load over a circular region with a diameter of 1 mm (estimated from the diameter of the string, approximately 1% of the wing's root chord). Because the stresses and strains in the membrane skin may approach infinity at the loading point, sufficient convergence of the finite element solution with grid density is demonstrated in Table 1. Results computed on the coarse mesh (Fig. 6) are within 1.5% of that computed upon the finer meshes.

Two material properties are needed: the elastic modulus and Poisson's ratio. The latter is fixed at 0.5, the commonly accepted value for incompressible rubbers [17]. Two separate values for the modulus were found to provide the best fit to the experimental data: 3 MPa was used to convert the prestrains of Fig. 5 into stresses, and 7 MPa was used for the calculation of stresses that developed due to the transverse point load. Theoretically, these two values should be equal: errors in the calculated prestrain (a particular problem with such small strains in the presence of substantial rigid-body motions is adhering the latex to the wing) or hyperelastic effects may cause the difference. The magnitude of the peak deformation (at the location of the concentrated load) is well-predicted for 1, 2, and 3 g of dead weight, though the model tends to slightly underpredict deformation aft of this loading point, toward the trailing edge, as seen in Fig. 7. Numerical membrane deformations from Fig. 7 are computed upon the coarse grid of Table 1. The method of using two distinct elastic moduli (one for the conversion of prestrains into prestresses and the other for computing aeroelastic deformation due to a pressure load) is used for the remainder of the results given next.

C. Validation of Wing Deformation

With the structural model properly tuned, we turn now to the static aeroelasticity of the membrane wing. Six elastic quantities can be measured/computed: three displacements (chordwise u , spanwise v , and transverse w) and three plane strains (chordwise ϵ_{xx} , spanwise ϵ_{yy} , and shear ϵ_{xy}). The transverse displacements and chordwise strains are thought to have the greatest effect upon the aeroelasticity and will be the focus of the following discussion. The strain fields given next are as a result of the aerodynamic loading and do not include the prestrain of Fig. 5.

The measured displacement field at a 0-deg angle of attack (Fig. 8) is entirely confined to the membrane skin, validating the assumption of a rigid (at least for the low dynamic pressures of the current

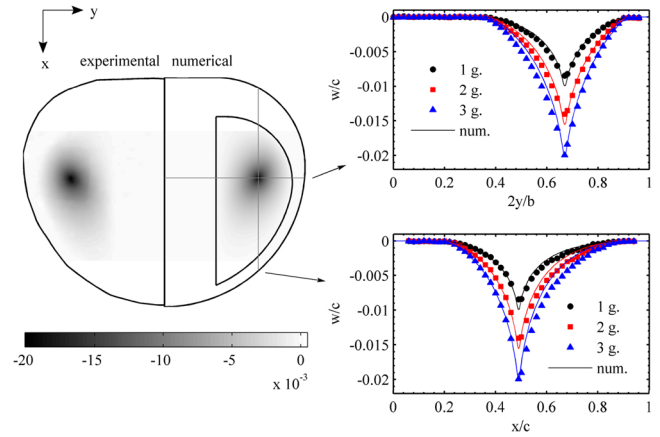


Fig. 7 Transverse displacements (normalized by the root chord) due to 1-, 2-, and 3-g weights hung from a string glued to the center of the membrane wing.

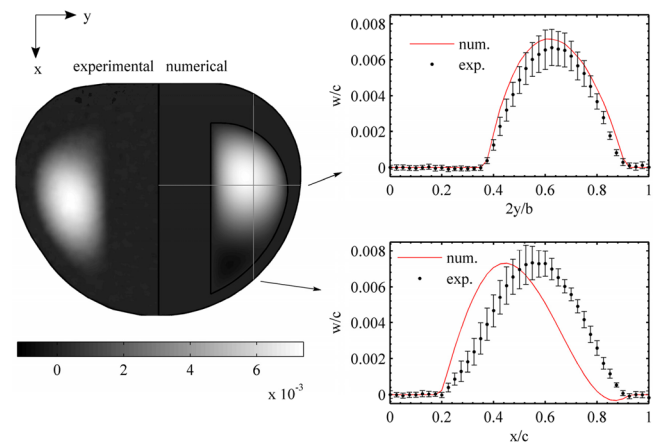


Fig. 8 Normalized transverse displacements; $\alpha = 0$ deg and $U_\infty = 13$ m/s.

application) carbon-fiber perimeter. Because both the leading and the trailing edges at each span station along the wing are fixed, the deformation can be adequately described as an aerodynamic twist. The transverse displacements are relatively small (almost three orders of magnitude less than the root chord), though they still affect the aerodynamics of the wing. At this low angle of attack, the magnitude of the deformation field is well-predicted by the model, though the location of the maximum displacement (corresponding to the camber of the wing) is computed far forward of the measured location. Furthermore, the model erroneously predicts a region of negative deformation (the membrane is pushed below the mean chord line) toward the trailing edge.

These discrepancies are likely due to the flow separation on both the lower surface (at the leading edge) and the upper surface of the wing (toward the trailing edge) typically associated with thin cambered wings at a 0-deg angle of attack. The low-Reynolds-number (10^5) laminar flow over the MAV wing easily separates and forms a recirculation bubble under an adverse pressure gradient, as detailed by Torres and Mueller [18]. Depending on a number of factors (including angle of attack), the laminar shear layer above the separation bubble may transition to turbulence, and the resulting momentum mixing can cause the flow to reattach aft of the bubble to form a turbulent boundary layer. A transition/turbulence module is not included in the CFD formulation, which relies purely on the laminar flow assumption. Therefore, any numerical simulations indicating reattached (or otherwise) laminar flow aft of a separation bubble must be viewed with suspicion and is thought to be a significant reason for the aeroelastic model's mixed predictive capabilities at this low angle of attack. Further information detailing the flow structures and separation behavior is detailed next.

Table 1 Mesh convergence: computed displacement at the force applied by the hanging weight

Mesh density	1 g	2 g	3 g
Coarse (639 nodes)	1.0343 mm	1.0462 mm	1.0478 mm
Medium (1161 nodes)	1.6175 mm	1.6337 mm	1.6361 mm
Fine (2193 nodes)	2.0866 mm	2.1060 mm	2.1088 mm

The error bars in the displacement measurements (Fig. 8) are estimated statistically (from ten measurements, spaced 1 s apart). At a 0-deg angle of attack, the peak uncertainty range is 0.2 mm, though the resolution error of the VIC system is estimated at 0.05 mm (found from the camera's field of view and pixel recording resolution [14]). The large displacement error bars are a result of unsteady flow; at low angles, the membrane wing experiences a self-excited vibration (visible in the wind tunnel). The VIC system used in this work is incapable of characterizing this vibration (estimated by Lian et al. [7] to be moving at 100 Hz): image sampling frequencies cannot exceed 2 Hz. Both the flow and structural solver assume steady flow conditions; this may also contribute to the modeling error at low angles, particularly if vortex shedding or membrane dynamics play a large role.

The measured chordwise strain field at 0 deg (Fig. 9) is similarly small, validating the use of the linear Hooke's law to convert strains into stresses, rather than a higher-fidelity hyperelastic model. The strains are only slightly above the resolution limit of the VIC system (~1000 $\mu\epsilon$). As such, the measured membrane strain field is fairly noisy. Furthermore, any flexural strains that may develop in the excessively stiff carbon-fiber wing skeleton are sure to fall below the resolution of the VIC system: strain measurements in this region are only noise. The model overpredicts the magnitude of the strain in the membrane, though it is able to capture the trends: a lobe of high extensional chordwise strain toward the membrane/weave boundary at the leading edge and low strain levels toward the trailing edge. Large strain gradients/magnitudes are measured at the border of the MAV wing; the VIC system has difficulties in computing the strain fields directly up to the edge of the area of interest and are erroneous.

The displacements at a 12-deg angle of attack (Fig. 10) are larger than before (two orders of magnitude less than the root chord). Both

the magnitude and the location of the peak membrane displacement show good correspondence between the experiment and simulation at 12 deg. The model's high predictive capability at this moderate angle of attack is likely due to the smooth flowfield; the flow over the bottom surface of the MAV wing is completely attached. As such, both the experimental and numerical transverse displacements are completely positive. The magnitude of the estimated displacement error is significantly smaller than that seen at the smaller angle; the flow is largely steady at 12 deg, and the error bars now reflect the inherent uncertainty/repeatability of the VIC system. The average displacement error bar is 0.05 mm long, consistent with the estimated resolution error of the VIC. The chordwise strain field at 12 deg (Fig. 11) is similarly well-predicted by the aeroelastic model. The lobe of high extensional chordwise strain is measured slightly aft of the membrane/weave boundary, whereas the model predicts peak strain directly on the boundary. The significantly higher strain levels (0.7% at 12 deg, up from 0.2% at 0 deg) provide a cleaner strain reading, though the VIC system again produces erroneous results at the edge of the MAV wing.

At a 30-deg angle of attack, the wing is in the poststall regime; the flow is completely separated over the top surface of the wing. The separated flow is very unsteady, as indicated by the large displacement error bars in Fig. 12. Nevertheless, the time-averaged wing displacement field is well-predicted by the steady aeroelastic model, in both the location and the magnitude of the peak displacement (~2 mm). The predicted strain field is less accurate at this angle. The measured chordwise strain (Fig. 13) is completely extensional, with the familiar lobe of high strain toward the leading edge. The model accurately predicts the lobe, but indicates a region of negative strain toward the trailing edge. This is probably Poisson strain, ostensibly due to high extensional strain in the span direction.

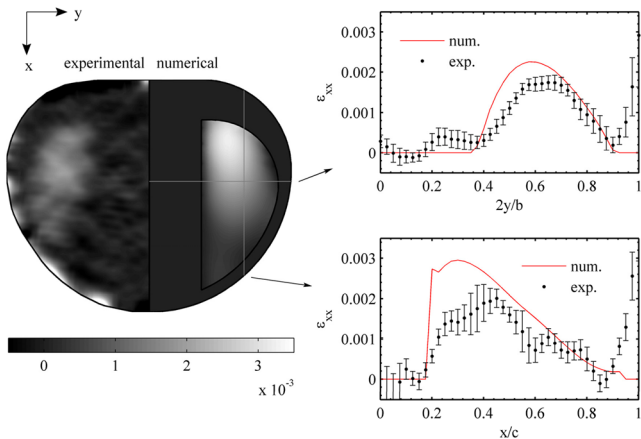


Fig. 9 Chordwise strains; $\alpha = 0$ deg and $U_\infty = 13$ m/s.

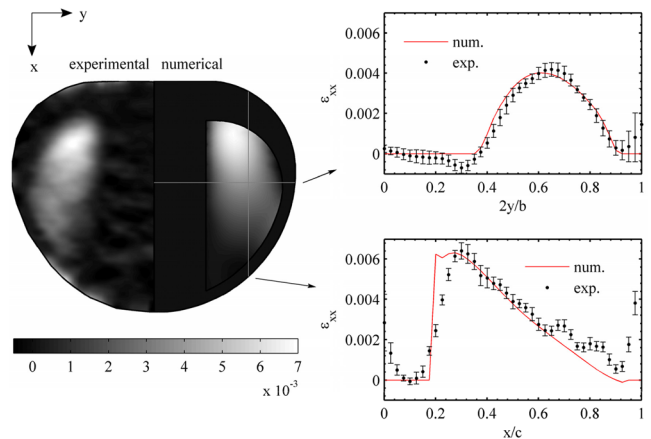


Fig. 11 Chordwise strains; $\alpha = 12$ deg and $U_\infty = 13$ m/s.

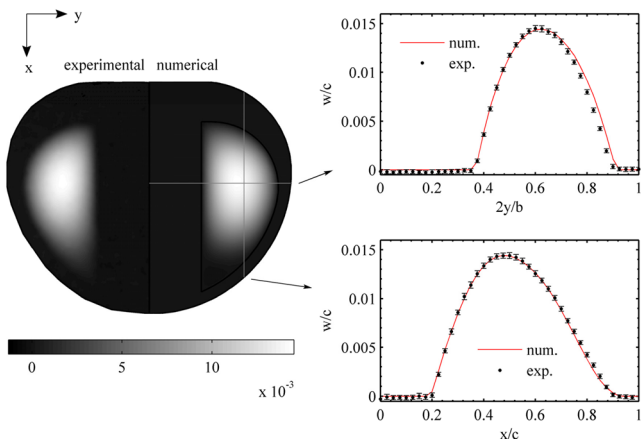


Fig. 10 Normalized transverse displacements; $\alpha = 12$ deg and $U_\infty = 13$ m/s.

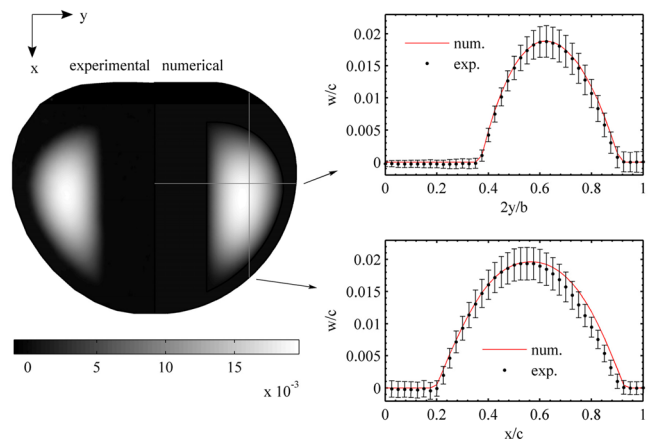


Fig. 12 Normalized transverse displacements; $\alpha = 30$ deg and $U_\infty = 13$ m/s.

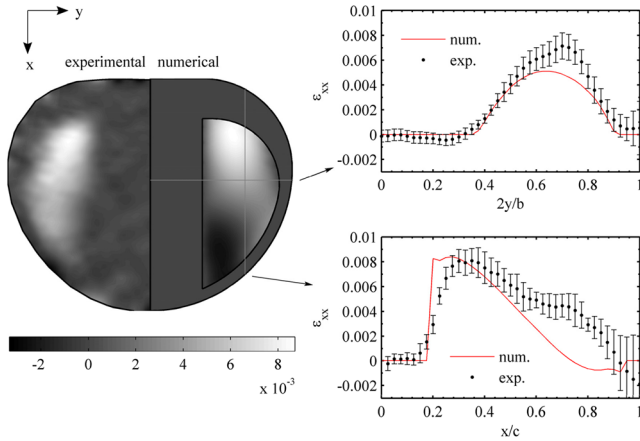


Fig. 13 Chordwise strains; $\alpha = 30$ deg and $U_\infty = 13$ m/s.

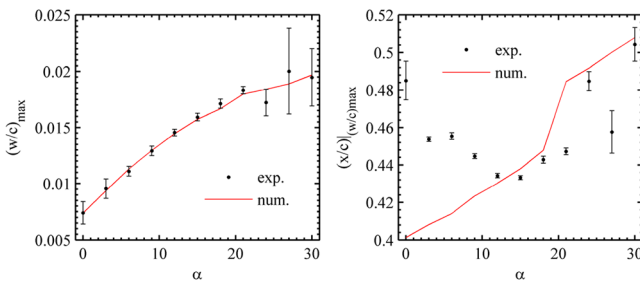


Fig. 14 Normalized peak displacement (left) and the normalized location of the peak (right) within the membrane skin; $U_\infty = 13$ m/s.

Wrinkling phenomena (the latex membrane cannot sustain a compressive stress [17]) may also be present, because the measured extensional strain in this region is very close to zero. Because a wrinkling module is not built into the finite element analysis, the model will instead predict membrane compression. A wrinkling pattern is not clearly visible from the measured displacement field (Fig. 12), though it is reported by Fink [8] for stalled membrane wings.

The maximum normalized displacement (essentially, the wing's adaptive camber) and the normalized location of this peak as a function of angle of attack can be seen in Fig. 14. The nonlinear behavior of the membrane deformation is clearly evident: up to the stall angle, the lift is linear with incidence (detailed next), whereas the transverse membrane inflation is not linear. This is a direct effect of the moderate amount of prestrain (Fig. 5) in the membrane wing. Larger prestrains will lead to a more linear inflation curve, though the peak displacement will be lower than that seen in Fig. 14. A completely linear stress-stiffening model could then be used, as is the approach of Sugimoto [6]. The size of the error bars indicates a region of steady flow at moderate angles of attack: between 6 and 21 deg (the latter is the approximate stall angle). For all angles, the aeroelastic model is capable of predicting the magnitude of the peak wing displacements to within experimental error bars. The initial decambering of the wing with the onset of stall is not predicted by the model, however.

The model is less successful at predicting the location of this peak displacement. The model places the camber 18% closer to the leading edge than the measured location at 0 deg. As the incidence increases, the model predicts that the camber moves aft, whereas the measured trend is opposite: toward the leading edge. As discussed previously, this is thought to be a result of the model's inability to characterize the separated flow patterns over the wing surface. The experimental and numerical data trends cross over at a 12-deg angle of attack, wherein the experimental trend reverses direction. This reversal is thought to coincide with the flow completely attaching itself to the lower wing surface. Above 12 deg, the aeroelastic model is able to predict the camber location with suitable accuracy.

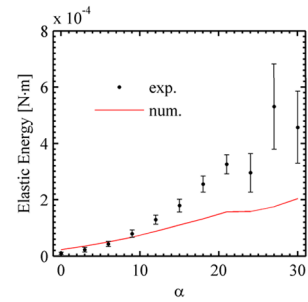


Fig. 15 Accumulated strain energy within the MAV wing; $U_\infty = 13$ m/s.

The elastic energy (the energy density is computed at each node from the strains and then integrated over the wing) within the wing can be seen in Fig. 15. As before, only the strains that accumulate during flight are considered, not the prestrains. Though the model's predictive capability is suitable at low angles of attack, the strain energy is slightly overpredicted. This is possibly due to the low strains that develop within the membrane, which are (as noted in Fig. 9) very close to the strain resolution of the VIC system. The model is able to predict the strain energy up to a moderate angle of attack (~ 9 deg), after which it significantly underpredicts the energy. This is most likely due to noise in the strain readings. Integrating over the entire wing provides an appreciable energy contribution from the strain spikes at the wing boundary and the noise in the carbon-fiber regions. The erroneous prediction of compressive strain toward the trailing edge of the membrane wing (Fig. 13) may also lead to the poor correspondence at high angles of attack.

D. Validation of Longitudinal Aerodynamic Coefficients

The coefficients of lift, drag, and pitching moment are given in Figs. 16 and 17 for both the membrane wing considered previously and a rigid wing. The latter has the same camber, dihedral, and planform shape as the undeformed membrane wing. The rigid wind-tunnel model is built from five layers of bidirectional carbon fiber and is constructed upon the same computer numerical control mold used for the membrane wing.

The computational fluid dynamics scheme detailed previously is able to accurately predict the prestall lift and drag over a rigid MAV wing: computed trends consistently fall within the experimental error

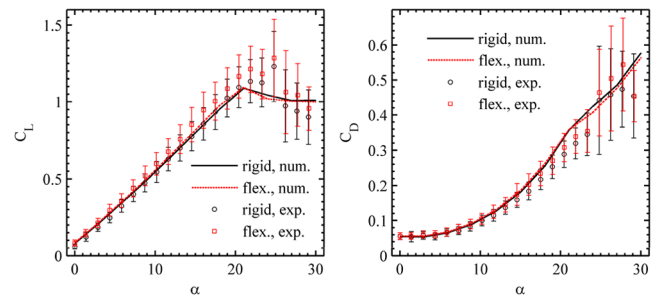


Fig. 16 Lift and drag for both a rigid and membrane MAV wing; $U_\infty = 13$ m/s.

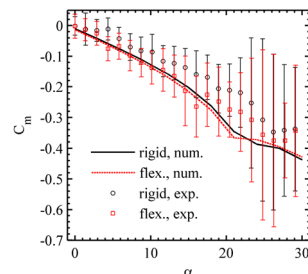


Fig. 17 Longitudinal static stability for both a rigid and membrane MAV wing; $U_\infty = 13$ m/s.

bars. The lift over the rigid wing is overpredicted by 11.3% at 3 deg and underpredicted by 1.24% at 18 deg. The drag is overpredicted by 8.51% at 3 deg and overpredicted by 11.9% at 18 deg. The stalling angle is underpredicted by 2 deg. Furthermore, both the model and experiment agree on a linear change in lift with angle of attack (pre stall). Some low-aspect-ratio wings display a nonlinear lift curve due to interference effects between the tip vortex swirling system and the wing circulation. Torres and Mueller [18] indicate that an imprecise cutoff ratio between linear and nonlinear lift- α behavior is roughly 1.2, which is the ratio for the MAV under consideration here. The shape of the wing planform can also affect the linearity.

Because the wing displacements in the previous section are relatively small, so are the changes in aerodynamic performance due to the membrane inflation. As expected, the lift, drag, and lift slope all increase (pre stall). The model generally predicts a smaller increase in aerodynamic force than that measured in the wind tunnel. For example, at an 18-deg angle of attack, the model predicts a 2.67% increase in lift due to the adaptive inflation, whereas the experimental data indicate a 7.52% increase. Similarly, the model predicts a 2.51% drag penalty, but a 7.58% penalty is measured at 18 deg. The aeroelastic model also incorrectly predicts lower lift and drag (compared with the rigid-wing aerodynamics) in the poststall regime, possibly due to simulated decambering of the membrane wing. Despite these errors in the aeroelastic simulations, the numerical data consistently lie within the experimental error bars for the membrane wing aerodynamics.

The longitudinal static stability is given in Fig. 17, in which the pitching moment is measured about the leading edge. The nose-down moment of the rigid MAV wing is consistently overpredicted by the CFD model (49.6% at an 18-deg angle of attack), though it still falls within the relatively large experimental error bars typically associated with pitching moment measurements. The ability of the rigid CFD model to accurately predict lift but not pitching moment is analogous to the data of Fig. 14; the magnitude of the deformation is well-predicted, but not necessarily the distribution of the displacement. The adaptive membrane inflation increases the nose-down pitching moment by increasing the force on the wing. At moderate angles, the moment arm is increased as well (Fig. 14). This increases the negative slope of the pitching moment curve and the static margin of the wing, representing the major benevolent characteristics of the adaptive wing. Stability concerns are a primary

target of design improvement from one generation of micro air vehicles to the next. The range of flyable c.g. locations on a MAV is generally a few millimeters long; meeting this requirement is a strenuous weight management challenge. As before, the aeroelastic model is able to predict the correct trend (5.36% increase in nose-down pitching moment with the membrane wing at 18 deg), but underpredicts the magnitude of the change (23.7% measured increase at 18 deg). Though not included in the wind-tunnel models, the wings of the actual flying micro air vehicles are equipped with a hinged trailing-edge portion acting as an elevator (as seen in Fig. 1) at a slightly negative deflection. Stable trim conditions are achieved during flight testing by tuning the proper combination of c.g. location and elevator-angle deflection at different propeller thrust levels.

E. Flow Structures

Streamlines at the root of a rigid MAV wing can be seen in Fig. 18 for three angles of attack (0, 15, and 30 deg). Both numerical data (computed using the CFD algorithm detailed previously) and experimental data (laser-based flow visualization) are given. A Model 95 Lexel continuous argon-ion 4.0-W laser is directed through a 1000-mm biconvex lens and a 25.4-mm semicylindrical lens to create a laser sheet. This sheet is then directed into the test section (Fig. 2), oriented parallel to both the incoming flow and the gravity vector, and focused on the root of the wing. This experimental setup affords flow visualization at other spanwise locations, but the strong crossflow elsewhere over the MAV wing limits the usefulness of this two-dimensional technique. Propylene glycol fog is injected into the tunnel as a seed particle. Images of the laser sheet are taken with a Nikon D70 camera and 200-mm AF Nikkor lens. Further information pertaining to the laser flow visualization for MAV applications is given by Sytsma [19].

Although the Reynolds number, planform shape, and airfoil are identical for the computational wing and the wind-tunnel model seen in Fig. 18, the latter has no dihedral. The airfoil shape at the root is simply extruded to both wingtips, which provides the camera with an unobstructed view across the span of the wing, thereby reducing overexposure. Because the wing studied in the rest of this work includes dihedral (7 deg toward the wingtips), the comparison of Fig. 18 is not completely ideal, though still beneficial in terms of model validation.

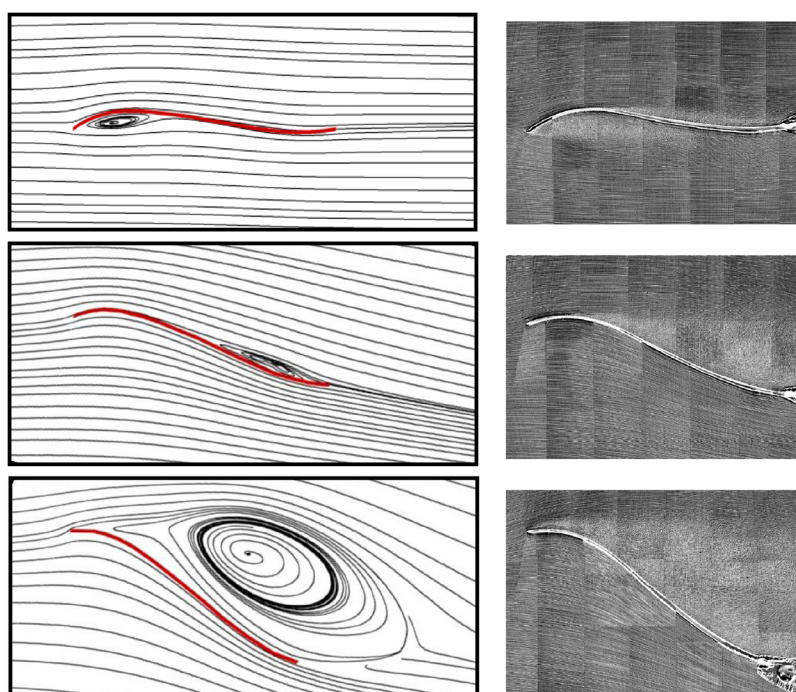


Fig. 18 Flow structures at the root of a rigid MAV wing; $\alpha = 0$ deg (top row), $\alpha = 15$ deg (middle row), and $\alpha = 30$ deg (bottom row); numerical results (left column) and experimental flow visualization mosaics (right column).

Both model and experiment indicate a large separation bubble on the lower surface of the wing toward the leading edge at a 0-deg angle of attack. The model's success in predicting both the size and location of this separation bubble perhaps signifies completely laminar flow over the bottom wing surface at this angle. The flow visualization also indicates that the flow separates over the location of maximum camber on the upper wing surface and reattaches toward the trailing edge. The numerical flow simulation also predicts a separation bubble at this angle, though significantly smaller (it cannot actually be seen in Fig. 18) and entirely confined toward the trailing edge. Similar prediction problems exist at the moderate angle of attack of 15 deg. Although both experimental and numerical data show that the flow on the underside of the wing is completely attached, the predicted zone of separated flow over the upper surface of the wing is again significantly underpredicted. Grid-refinement studies have indicated that adding more nodes to the structured mesh seen in Fig. 3 (from 210,000 to a million) can increase the size of the computed separation bubbles; grid-independent solutions are difficult to obtain at such low Reynolds numbers. The lack of a transition/turbulence model probably also prevents a better correlation between the experiment and the model; the visualization mosaic at a 15-deg angle of attack shows that the flow does not have sufficient room to reattach to the upper wing surface, whereas the numerical flow does have sufficient room. At a 30-deg angle of attack, both the model and experiment show completely separated flow over the upper wing surface, starting at the leading edge.

Because the previous sections have provided confidence in the aeroelastic model's ability to predict deformed wing shapes, accumulated membrane strains, and aerodynamic forces/moments, attention is now turned to numerical data that cannot (with the current experimental apparatus) be verified in the laboratory. The simulated pressure distributions over the top and bottom wing surfaces for both the rigid and the membrane wing are given in the following figures for 0- and 15-deg angles of attack. For both angles, the low-pressure region on the top surface toward the wingtip is evident, caused by the core of the tip vortex swirling system. The strength of this system is due to the low-aspect-ratio nature of the wing and is seen to increase with angle of attack. The pressure drops at the tips of the membrane wings are slightly smaller than those found in the corresponding rigid wings (from -295.6 to -287.9 Pa at 15 deg). This would perhaps indicate that the strain energy in the adaptively inflated membrane is removing energy from the vortex structure in the wake, thus decreasing the induced drag. This would merely be a drag redistribution, because the total drag seen in Fig. 16 is clearly higher for the membrane wing. The data do indicate that the rolling instabilities associated with low-aspect-ratio wings may be improved with flexible membranes.

At the low angle attack (0 deg, shown in Figs. 19 and 20), flow over the rigid wing is prone to separation at a number of locations, as discussed previously. The onset of pressure recovery over the top surface occurs at $x/c = 0.15$ and is followed by an adverse gradient. This gradient is exacerbated by the presence of a high-pressure region over the recurved portion of the airfoil. The resulting separation bubble in this region is not typically evident in similar computations involving singly curved wings at low angles of attack [7]. A second adverse pressure gradient is seen between the leading edge and the quarter-chord of the lower surface of the rigid MAV wing, leading to the large separation bubble. Aft of this computed

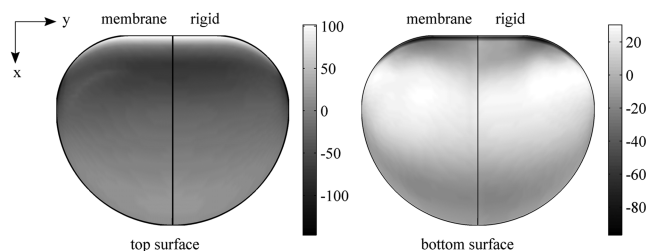


Fig. 19 Computed pressure (Pa); $\alpha = 0$ deg and $U_\infty = 13$ m/s.

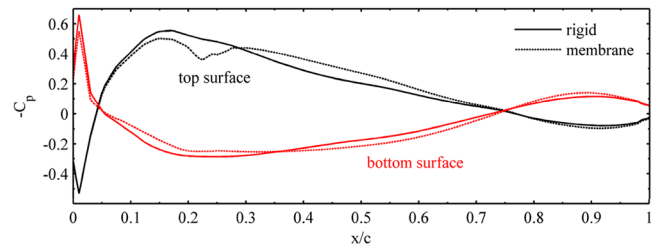


Fig. 20 Computed pressure coefficients at $2y/b = 0.7$; $\alpha = 0$ deg and $U_\infty = 13$ m/s.

bubble, the flow accelerates under the recurved area of the wing, resulting in a pressure drop.

When the inflated membrane shape is included in the flow structure at 0-deg simulations, the tangent discontinuity in the wing surface at the membrane/weave boundary forces the flow over the top surface to decelerate (rapidly change direction). This causes the pressure spike clearly evident in Fig. 20. The flow then accelerates over the inflated membrane shape (the increased camber leads to higher pressures than that seen in rigid-wing computations, increasing the nose-down pitching moment and thus the static margin) before separating, as in the rigid-wing case. On the bottom surface of the membrane wing, flow still separates at the leading edge, but then accelerates into the cavity of the inflated shape, resulting in a small area of lower pressure. The region beneath the inflated membrane is massively separated, until the flow again accelerates under the recessed portion of the wing and into the freestream. The pressure drag over the membrane wing is increased by this larger zone of separated flow, as well as by the pressure spike at the membrane/weave boundary (a considerable portion of which is directed in the drag direction). As on the top surface of the membrane wing, the adaptive inflation pushes the high-pressure region slightly aft, improving static stability.

At a 15-deg angle of attack (Figs. 21 and 22), the favorable pressure gradient over the lower surface of the rigid MAV wing indicates a smoothly accelerated flow from the leading edge to the trailing edge (as seen in Fig. 18). As expected, the magnitude of the suction at the wingtips is much larger at the moderate angle of attack, accompanied by an increase in induced drag. The flow over the top of the rigid wing remains separated, though both the size of the computed adverse pressure gradient and the increased incidence signify a larger separated zone than that seen in computations at 0 deg. For the membrane wing at 15 deg, the pressure spike on the top surface is very pronounced, as is an extended low-pressure zone that

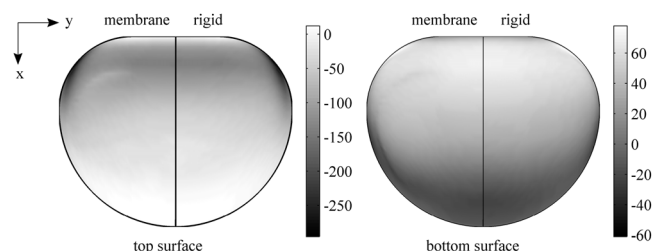


Fig. 21 Computed pressure (Pa); $\alpha = 15$ deg and $U_\infty = 13$ m/s.

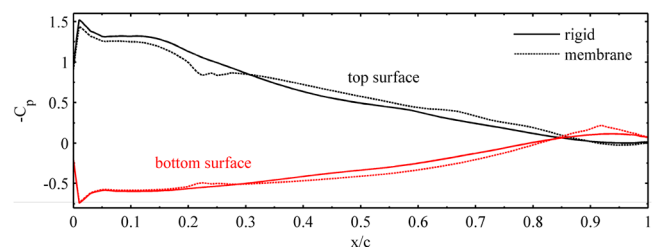


Fig. 22 Computed pressure coefficients at $2y/b = 0.7$; $\alpha = 15$ deg and $U_\infty = 13$ m/s.

develops at the membrane/weave boundary toward the trailing edge of the lower surface, which develops as the flow escapes from underneath the inflated membrane cavity.

V. Conclusions

A series of wind-tunnel tests were performed to validate a static aeroelastic model for low-Reynolds-number, low-aspect-ratio membrane micro air vehicle wings with adaptively inflating camber. A visual image correlation system in conjunction with a standard strain-gage sting balance were used to measure the wing loads, displacements, and strains for a range of pre- and poststall angles of attack. Modeling efforts included coupling a membrane finite element with geometric nonlinearities to a laminar Navier–Stokes solver. A comparison of experimental and numerical deformed membrane profiles indicates poor predictive capabilities of the steady aeroelastic solver at low angles of attack; massive separation under the wing leads to unsteady flow phenomena. A comparison of numerical and experimental (via laser flow visualization) flow structures shows discrepancies in the flow separation/reattachment behavior, most likely a result of laminar–turbulent transition that occurs above a separation bubble at low Reynolds numbers.

Good correlation in wing displacements and strains is attainable at moderate angles (where the flow is steady) and even at poststall angles (where the flow is not steady). The Navier–Stokes solver is able to predict the longitudinal aerodynamics over a rigid MAV wing within the experimental error for the entire α sweep. The aeroelastic solver correctly indicates the trends in aerodynamic performance with adaptive camber adjustment (increased lift, lift slope, and drag), though the magnitude of the shift is generally underpredicted. Turbulence effects, unsteady flow, and membrane wrinkling are all identified as candidates for upgrading the model fidelity. An examination of the computed pressure distributions identifies several key aeroelastic effects: decreased tip vortex strength, pressure spikes and flow deceleration at the tangent discontinuity of the inflated membrane boundary, and an adaptive shift of high-pressure (on the bottom surface) and low-pressure (on the top surface) regions toward the trailing edge, thereby increasing the nose-down pitching moment and the static margin.

Acknowledgments

This work was jointly supported by the U.S. Air Force Research Laboratory and the U.S. Air Force Office of Scientific Research under F49620-03-1-0381 with Todd Combs, Sharon Heise, and Johnny Evers as project monitors. The authors would also like to acknowledge the technical contributions and funding of Martin Waszak at the NASA Langley Research Center.

References

- [1] Ifju, P., Ettinger, S., Jenkins, D., and Martinez, L., “Composite Materials for Micro Air Vehicles,” *SAMPE Journal*, Vol. 37, No. 4, 2001, pp. 7–13.
- [2] Jackson, P., “A Simple Model for Elastic Two-Dimensional Sails,” *AIAA Journal*, Vol. 21, No. 1, 1983, pp. 153–155.
- [3] Smith, R., Shyy, W., “Computation of Aerodynamic Coefficients for a Flexible Membrane Airfoil in Turbulent Flow: A Comparison with Classical Theory,” *Physics of Fluids*, Vol. 8, No. 12, 1996, pp. 3346–3353.
doi:10.1063/1.869122
- [4] Boudreault, R., “3-D Program Predicating the Flexible Membrane Wing’s Aerodynamic Properties,” *Journal of Wind Engineering and Industrial Aerodynamics*, Vol. 19, No. 1, 1985, pp. 277–283.
doi:10.1016/0167-6105(85)90065-0
- [5] Jackson, P., and Christie, G., “Numerical Analysis of Three-Dimensional Elastic Membrane Wings,” *AIAA Journal*, Vol. 25, No. 5, 1987, pp. 676–682.
- [6] Sugimoto, T., “Analysis of Circular Elastic Membrane Wings,” *Japanese Society for Aeronautical and Space Sciences Journal*, Vol. 39, No. 447, 1991, pp. 180–187.
- [7] Lian, Y., Shyy, W., Vieru, D., and Zhang, B., “Membrane Wing Aerodynamics for Micro Air Vehicles,” *Progress in Aerospace Sciences*, Vol. 39, No. 6, 2003, pp. 425–465.
doi:10.1016/S0376-0421(03)00076-9
- [8] Fink, M., “Full Scale Investigation of the Aerodynamic Characteristics of a Model Employing a Sailingwing Concept,” NASA TN D-4062, 1967.
- [9] Greenhalgh, S., and Curtiss, H., “Aerodynamic Characteristics of a Flexible Membrane Wing,” *AIAA Journal*, Vol. 24, No. 4, 1986, pp. 545–551.
- [10] Galvao, R., Israeli, E., Song, A., Tian, X., Bishop, K., Swartz, S., and Breuer, K., “The Aerodynamics of Compliant Membrane Wings Modeled on Mammalian Flight Mechanics,” 36th AIAA Fluid Dynamics Conference and Exhibit, San Francisco, AIAA Paper 2006-2866, 2006.
- [11] Fleming, G., Bartram, S., Waszak, M., and Jenkins, L., “Projection Moiré Interferometry Measurements of Micro Air Vehicle Wings,” SPIE International Symposium on Optical Science and Technology, San Diego, CA, SPIE–The International Society for Optical Engineering, Paper 4448-16, 2001.
- [12] DeLuca, A., Reeder, M., Michael, V., Freeman, J., Bautista, I., and Simonich, M., “Experimental Investigation into the Aerodynamics of a Flexible and Rigid Micro Air Vehicle,” 24th AIAA Aerodynamic Measurement Technology and Ground Testing Conference, Portland, OR, AIAA Paper 2004-2396, 2004.
- [13] Sutton, M., Cheng, M., Peters, W., Chao, Y., and McNeill, S., “Application of an Optimized Digital Correlation Method to Planar Analysis,” *Image and Vision Computing*, Vol. 4, No. 3, 1986, pp. 143–151.
doi:10.1016/0262-8856(86)90057-0
- [14] Schreier, H., Braasch, J., and Sutton, M., “Systematic Errors in Digital Image Correlation Caused by Intensity Interpolation,” *Optical Engineering*, Vol. 39, No. 11, 2000, pp. 2915–2921.
doi:10.1117/1.1314593
- [15] Thakur, S., Wright, J., and Shyy, W., “STREAM: A Computational Fluid Dynamics and Heat Transfer Navier–Stokes Solver: Theory and Applications,” Streamline Numerics, Inc., Gainesville, FL, 2002.
- [16] Cook, R., Malkus, D., Plesha, M., and Witt, R., *Concepts and Applications of Finite Element Analysis*, Wiley, New York, 2002.
- [17] Jenkins, C. (ed.), *Gossamer Spacecraft: Membrane/Inflatable Structure Technology for Space Applications*, Vol. 191, AIAA Progress in Astronautics and Aeronautics Series, AIAA, Reston, VA, 2001.
- [18] Torres, G., and Mueller, T., “Low Aspect Ratio Aerodynamics at Low Reynolds Numbers,” *AIAA Journal*, Vol. 42, No. 5, 2004, pp. 865–873.
- [19] Systema, M., “Aerodynamic Flow Characterization of Micro Air Vehicles Utilizing Flow Visualization Methods,” M.S. Thesis, Department of Mechanical and Aerospace Engineering, Univ. of Florida, Gainesville, FL, 2006.

E. Livne
Associate Editor